Supplementary Materials for

Topology and Dynamics of Active Nematic Vesicles

Felix C. Keber, Etienne Loiseau, Tim Sanchez, Stephen J. DeCamp, Luca Giomi, Mark J. Bowick, M. Cristina Marchetti, Zvonimir Dogic and Andreas R. Bausch

correspondence to: abausch@mytum.de

This PDF file includes:

Other Suplementary Materials for this manuscript includes the following:

Supplementary Materials

Contents

Materials and Methods

Methods summary

Tubulin purification, microtubule polymerization, kinesinstreptavidin complexes and preparation of active microtubule-kinesin mixtures were performed as previously published (*19*). The presence of an ATP regeneration system ensures that molecular motors move at constant velocity and that the activity-driven microscopy dynamics remains unchanged. The active microtubule mixtures were encapsulated into vesicles using the continuous droplet interface crossing encapsulation method (cDICE) (*25*), for which it is necessary to increase the weight of the water phase solution by the addition of 300mM Sucrose. The composition of the membrane is 95 % Egg PC and 5 % PEG2000 PE to prevent protein adsorption. The ambient buffer has the same composition as the active sample where the osmolarity was adjusted with Glucose. Coverslips surfaces were coated with either casein or an acrylamide-brush to suppress vesicle adhesion to the glass surface (*19*). Image stacks were taken with a confocal microscope. Defects were identified and their dynamics was tracked by least distance algorithms using custom software written in ImageJ and Matlab.

Reagents

L-α-Phosphatidylcholine (Egg PC) lipids are ordered from Sigma (P3556) in powder form and dissolved at 50 mg/ml in a chloroform/methanol mixture 9/1 v/v. This stock solution is used three weeks after dissolution. 1,2-dipalmitoyl-sn-glycero-3-phosphoethanolamine-N-[methoxy(polyethylene glycol)-2000] (PEG2000 PE) lipids are ordered from Avanti Polar Lipids (880160C), dissolved at 10 mg/ml in chloroform. Mineral oil is from Sigma (M3516).

Active mixture

Tubulin purification and microtubule polymerization, kinesin-streptavidin complexes and active microtubule-kinesin mixtures where performed or prepared as previously published (*19*). Tubulin (from bovine brain) was polymerized for 2 days to an average length of 1.5m. Biotinylated kinesin (K401, D.melanogaster) and Streptavidin (Invitrogen, S-888) were incubated to build complexes at least 10 min before use. The buffer solution was changed to contain now additionally 300mM Sucrose to increase the weight of the vesicles. The microtubules used in the ATP experiments were polymerized in a similar manner as previously, but at a higher tubulin concentration and in the absence of glycerol. The polymerization mixture is 5μl (14mg ml^{-1}) unlabeled tubulin, 1.25μl (6mg ml^{-1}) Alexa-647-labelled tubulin (28% labeling efficiency), 2.37μl M2B buffer, 0.58μl GpCpp (10 mM) (Jena Biosciences, NU-405L), and 0.48μl DTT (20 mM) for a final tubulin concentration of 8mg ml^{-1} and an average length of 1μm.

Vesicles production

Vesicles are produced using the continuous droplet interface crossing encapsulation (cDICE) method described in (*25*). Briefly, it consists of a cylindrical rotating chamber, successively filled with a glucose solution to collect the vesicles, a lipid in oil solution to saturate the oil/water (O/W) interfaces, and decane as the continuous phase in which droplet are produced. The solution containing the microtubules and motors is injected from a glass capillary by inserting the capillary's tip in the decane. Due to the centrifugal force, droplets detach from the tip. The droplets then move through the lipid in oil solution where they get coated by a first lipid monolayer and then by a second lipid monolayer while crossing the O/W interface. The two monolayers zip together to form a bilayer. Vesicles are collected in the glucose solution which is sucked with a micropipette once the chamber is stopped. For the process to succeed, the osmolarity of the encapsulated solution and glucose solution have to be matched. The composition of the membrane is 95% Egg PC and 5% PEG2000 PE to prevent protein adsorption.

Imaging

Confocal fluorescence microscopy was performed on a Leica SP5 confocal microscope using a 63x oil immersion objective and if necessary using a resonance scanner (Leica Microsystems, Wetzlar, Germany). Coverslips were coated with casein (Sigma Aldrich) or an acrylamide-brush (as stated before in Ref. (*19*)) and a cylindrical polydimethylsiloxane (PDMS) chamber (20 μl) was placed on them. After injection of the vesicle solution the chamber was closed by another coverslip.

ATP concentration series

One batch of protein solution was used to obtain the systematic dependence of the speeds on the ATP concentration. The absolute speed of the active solutions depends on the exact batch used and can vary from batch to batch by a factor of 2, presumably due to the exact morphology of the bundles produced during the polymerization.

Deswelling experiment

The observation chamber for a deswelling experiment consists of a two level chamber (2x20 μl) made of PDMS. 20 μl of glucose solution containing vesicles are poured in the first level. Then a membrane (Millipore Durapore® 0.1 μm) is placed on the top and the second level is filled with 20 μl of a glucose solution whose the osmolarity is 20% higher. While the hypertonic solution diffuses through the membrane, the vesicles undergo a water efflux to equilibrate the surrounding osmolarity. This results in vesicles with a final reduced volume of 0.9.

Size dependence experiment

A large batch ($N = 168$) of vesicles in the range of 8-20 μm radius was evaluated manually. The spindle configuration was not included into the histogram, due to its metastable behavior. The morphologies observed in all other batches, where only single vesicles were acquired ($N \sim 50$), fit into that histogram and above $r = 20$ μm all observed vesicles showed four $+1/2$ defects, summarized in the last bin of the histogram.

Image analysis

Vesicle surfaces or maximum perimeters were extracted, ellipse analysis and xyz-hemisphere projections were performed by home-made Fiji/imageJ programs. Defect identification was performed manually in six hemisphere projections, tracking and further analysis were using MATLAB (The Mathworks) programs.

Supplementary Text

Self-Propelled Particles Model

It was suggested that $+1/2$ disclinations in active nematics can be described as self-propelled particles moving at a constant velocity v_0 proportional to the activity (*21*). Fueled by the activity of the motors, the highly distorted configuration of the nematic director around an isolated disclination builds-up a non-uniform active stress $\boldsymbol{\sigma}^{\mathrm{active}} = a\boldsymbol{Q}$, where $\boldsymbol{Q}$ is the nematic tensor and a a phenomenological parameter with dimensions of stress that embodies all the active contributions (notice that in the present convention $a < 0$ for extensile systems). In the presence of a $+1/2$ disclination such an active stress drives the flow shown in Fig. S2a. The director field surrounding the defect is then advected by such a self-generated flow, which results in a motion of the defect core at constant speed $v_0 \approx |a|R/\eta$. Here R is a typical length scale in the system which here can be identified with the sphere radius. Unlike $+1/2$ disclinations, $-1/2$ disclinations produce a symmetric flow that stirs the fluid in the neighborhood of the defect without producing any net motion (Fig. S2b).

Generalizing this approach to the spherical case, each defect may be described by a position vector on the sphere $\boldsymbol{r} = \boldsymbol{r}(\theta, \phi)$, where θ and ϕ are the usual spherical coordinates, and an orientation $\boldsymbol{u}$. The positional dynamics of the i-th defect is then governed by the equations:

$$\frac{d\boldsymbol{r}_i}{dt} = v_0 \boldsymbol{u}_i + \zeta_t^{-1} \boldsymbol{F}_i \,, \qquad 1 \leq i \leq 4 \,. \tag{1}$$

Here v_0 is a constant velocity due to activity, ζ_t is a translational friction and $\boldsymbol{F}_i = -\nabla_i E$, with $\nabla_i = R^{-1}(\partial/\partial\theta_i + 1/\sin\theta_i\, \partial/\partial\phi_i)$ and R the radius of the sphere, is the total elastic force acting on each defect due to all the others. The energy E is given by (*2*) (*6*):

$$E = -\pi K \sum_{i<j} k_i k_j \log(1 - \cos\beta_{ij}) + N E_{\mathrm{self}} \,, \tag{2}$$

where k_i is the turning number of the $i-$th defect ($k_i = 1/2$ in our case), K the Frank elastic constant expressing the orientational stiffness of the nematic phase, $\cos\beta_{ij} = \cos\theta_i \cos\theta_j + \sin\theta_i \sin\theta_j \cos(\phi_i - \phi_j)$, and $E_{\rm self}$ is the position-independent defect self-energy.

In order to express Eq. (1) in spherical coordinates, we introduce an orthonormal basis of tangent vectors on the sphere:

$$\boldsymbol{e}_\theta = (\cos\theta\cos\phi, \cos\theta\sin\phi, -\sin\theta) \ , \qquad\qquad \boldsymbol{e}_\phi = (-\sin\phi, \cos\phi, 0) \ .$$

The right-hand side of Eq. (1) can then be expressed in local coordinates as:

$$\frac{1}{R}\frac{d\boldsymbol{r}}{dt} = \dot\theta\, \boldsymbol{e}_\theta + \dot\phi \sin\theta\, \boldsymbol{e}_\phi \ . \tag{3}$$

Calculating the forces yields, after some algebraic manipulation:

$$\boldsymbol{f}_i = -\frac{\pi K}{R^2} \sum_{j\neq i} \frac{k_i k_j}{1-\cos\beta_{ij}}\, \boldsymbol{\Pi}_i \cdot \boldsymbol{r}_j \ , \tag{4}$$

where $\boldsymbol{\Pi}_i = \boldsymbol{e}_{\theta i}\, \boldsymbol{e}_{\theta i} + \boldsymbol{e}_{\phi i}\, \boldsymbol{e}_{\phi i}$ is the tangent projection operator that projects the position vector $\boldsymbol{r}_j$ on the plane tangent to the sphere at the point $\boldsymbol{r}_i$. Combining Eqs. (3) and (4), and writing:

$$\boldsymbol{u}_i = \cos\psi_i\, \boldsymbol{e}_{\theta i} + \sin\psi_i\, \boldsymbol{e}_{\phi i} \ , \tag{5}$$

the equations for the spherical angles θ_i and ϕ_i become:

$$\frac{d\theta_i}{dt} = \frac{v_0}{R}\, \cos\psi_i - \frac{\pi K}{\zeta_t R^2} \sum_{j\neq i} \frac{\boldsymbol{e}_{\theta i}\cdot\boldsymbol{r}_j}{1-\cos\beta_{ij}} \ , \tag{6a}$$

$$\frac{d\phi_i}{dt} = \frac{1}{\sin\theta_i}\left[\frac{v_0}{R}\, \sin\psi_i - \frac{\pi K}{\zeta_t R^2} \sum_{j\neq i} \frac{\boldsymbol{e}_{\phi i}\cdot\boldsymbol{r}_j}{1-\cos\beta_{ij}}\right] , \tag{6b}$$

where the product $k_i k_j = 1/4$ has been incorporated in the definition of the Frank constant K. Analogously, the equation for the angle ψ has the form:

$$\zeta_r \frac{d\psi_i}{dt} = M_i \ , \tag{7}$$

where M_i is the torque experienced by the $i-$th disclination and ζ_r is a rotational drag. As for Eqs. (6), inertial effects are neglected. The expression for the torque M_i is obtained by adapting to the sphere the expression derived in the planar case (see Sec.). This yields:

$$\zeta_r \frac{d\psi_i}{dt} = -\pi K \sum_{j\neq i} \frac{\boldsymbol{u}_i^\perp \cdot \boldsymbol{u}_j'}{1-\boldsymbol{u}_i\cdot\boldsymbol{u}_j'} \ , \tag{8}$$

where $\boldsymbol{u}_i^{\perp} = -\sin\psi_i\,\boldsymbol{e}_{\theta i} + \cos\psi_i\,\boldsymbol{e}_{\phi i}$ and $\boldsymbol{u}'_j$ is the unit vector obtained by parallel-transporting $\boldsymbol{u}_j$ from $\boldsymbol{r}_j$ to $\boldsymbol{r}_i$ along the great circle connecting the two points (Fig.S3). Explicitly:

$$\boldsymbol{u}'_j = (\boldsymbol{u}_j \cdot \boldsymbol{t}_j)\,\boldsymbol{t}_i + (\boldsymbol{u}_j \cdot \boldsymbol{n}_j)\,\boldsymbol{n}_i \ , \tag{9}$$

where $\boldsymbol{t}$ and $\boldsymbol{n}$ are respectively the tangent and tangent-normal vector of the Darboux frame attached to the great circle connecting $\boldsymbol{r}_j$ with $\boldsymbol{r}_i$. The tangent vectors $\boldsymbol{t}_i$ and $\boldsymbol{t}_j$ can be obtained by projecting the chord $\boldsymbol{r}_i - \boldsymbol{r}_j$ to the tangent plane and thus:

$$\boldsymbol{t}_j = \frac{\boldsymbol{\Pi}_j \cdot \boldsymbol{r}_i}{|\boldsymbol{\Pi}_j \cdot \boldsymbol{r}_i|} \ , \qquad \boldsymbol{t}_i = -\frac{\boldsymbol{\Pi}_i \cdot \boldsymbol{r}_j}{|\boldsymbol{\Pi}_i \cdot \boldsymbol{r}_j|} \ ,$$

where we used the fact that $\boldsymbol{\Pi}_i \cdot \boldsymbol{r}_i = 0$. The normal vectors $\boldsymbol{n}_i$ and $\boldsymbol{n}_j$ can be found by a simple 90° rotation about the sphere normal vector: i.e. $\boldsymbol{n}_i = (\boldsymbol{r}_i/R) \times \boldsymbol{t}_i$ and $\boldsymbol{n}_j = (\boldsymbol{r}_j/R) \times \boldsymbol{t}_j$.

Numerical solution

To render Eqs. (6) and (8) dimensionless we can rescale all distances by the sphere radius R. A suitable time unit is given by the relaxational time scale associated with the defects positions, $\tau = \zeta_t R^2/(\pi K)$. Similarly $v_0 \to v_0/(R/\tau)$. With this choice of units Eqs. (6) and (8) have been integrated numerically using a fourth order Runge-Kutta method with time step $\Delta t = 10^{-3}$. The defects are initially positioned randomly near the equator and also randomly oriented.

For zero activity ($v_0 = 0$) the defects move solely as a consequence of the passive forces and torques. These drive the system to rapidly relax to the lowest energy state, with the defect sitting at the vertices of a regular tetrahedron (Fig. S4) [1]. The orientations $\boldsymbol{u}_i$ are organized in two coplanar pairs forming two perpendicular planes. For small non-zero activity, the stationary solution continues to be stable, but it is no longer regular and the original tetrahedral configuration is replaced by a skewed tetrahedron of increasingly high eccentricity. To characterize this behavior we have measured the average angle between pair of defects:

$$\langle\alpha\rangle = \frac{1}{6}\sum_{i<j} \arccos\left(\frac{\boldsymbol{r}_i \cdot \boldsymbol{r}_j}{R^2}\right) \ . \tag{10}$$

For a perfect tetrahedral configuration the defects are equally spaced and $\langle\alpha\rangle_{\rm tetra} = \arccos(-1/3) = 109.5°$. Fig. S5 shows a plot of the average angle $\langle\alpha\rangle$ as a function of the defect velocity v_0. The data show a rapid increase of the angle as the value $v_0^* \approx 0.25$ is approached. This marks the instability of the (distorted) tetrahedral configuration to the oscillatory regime.

Upon increasing v_0 above v_0^*, the dynamics is characterized by a collective motion of the four defects. The defects appear grouped in two pairs (see Fig. 3 in the main text and Movie S2). In each

[1] Note that the equilibrium configuration depends on the ratio of the elastic constants for splay and bend. In particular the tetrahedron may be distorted, depending on the values of these two Frank elastic constants. Here they are taken to be equal.

pair the defects are 180° apart and revolve at constant angular velocity around the pair's center of mass. During each revolution the defects go from the tetrahedral configuration (Fig. S6a inset) to an intermediate planar configuration in which the defects are equally spaced along a great circle, to a new tetrahedral configuration inverted with respect to the initial one. Simultaneously, the average angular distance varies from 109.5° to 120° (Fig. S6a and Fig. 3 in the main text), the latter being the average angular distance associated with the planar configuration (i.e. each defect is separated by 90° from its two neighbors and by 180° from the remaining defect and thus $\langle\alpha\rangle_{\rm planar} = 120^\circ$).

The origin of this oscillatory behavior is related to the lag in the dynamics of defect core and orientation. This behavior is embodied in the dimensionless number

$$\Gamma = \frac{\zeta_t R^2}{\zeta_r} \,, \tag{11}$$

representing the ratio between translational and rotational friction. For $\Gamma \ll v_0$ the defects quickly reach the distorted tetrahedral configuration and eventually reorient to form the optimal baseball texture described earlier. For $\Gamma \gg v_0$, on the other hand, the reorientation occurs already as the defects are approaching the tetrahedral configuration, causing them to turn around and get locked in a periodic orbit. In the experimental system the dynamics of the defect orientation is presumably much faster than the translational dynamics of the core as the core region is depleted of filaments and thus the motion of the core implies an actual transfer of mass while the orientational dynamics does not.

Fig. S6b shows a plot of the oscillation frequency versus v_0 obtained from a numerical integration of Eqs. (6) and (8). For large activity values the frequency scales linearly with v_0 as one would expect from inspection of Eqs. (6). For small v_0, on the other hand, the data show a slight sub-linear dependence on v_0. This can be understood as follows. As explained earlier, the defects form two pairs revolving around each of the poles. The time needed to perform a full revolution is $T = \Delta r/v_0$, with Δr the radius of the circular orbit set by the balance between defect repulsion and propulsion. The slight sub-linear dependence at small v_0 indicates that Δr increases with v_0 until reaching a plateau.

From Ref. (*21*) we expect $v_0 \approx aR/\eta$, with η the shear viscosity of the suspension. For large values of v_0 the frequency of oscillations increases linearly with v_0 and is expected to be of order v_0/R and hence independent of the radius of the vesicle. Neglecting the effect of activity on the shear viscosity η of the suspension we then expect the frequency to increase linearly with activity, which in the experiments is set by the rate of ATP consumption.

Rotational dynamics of planar nematic disclinations

Here we provide a derivation of the expression for the effective torque used in Eq. (8).The angular interaction between two $+1/2$ defect of arbitrary orientation will arise from deformations of the hydrodynamic elastic energy. Here we propose a possible derivation that relies on the method of introducing two defects dipoles. When two $+1/2$ disclinations in a two-dimensional nematic liquid crystal are close to each other (Fig. S7, left), the relaxation of the director field produces a rotation of their symmetry axis $\boldsymbol{u}$. Such a rotation can be ascribed to an effective *torque* exerted by the disclinations

on each other. Similarly, one can expect the dynamics of the orientation $\boldsymbol{u}_i = (\cos\psi_i, \sin\psi_i)$, with $i = 1,\ 2$, to obey to an equation of the form

$$\zeta_r \frac{d\psi_i}{dt} = M_i \ , \tag{12}$$

where M_i is the torque experienced by the $i-$th disclination and ζ_r is a rotational drag. Inertial effects have been neglected from Eq. (12), so that the reorientation of the director fields stops when the torque vanishes.

To calculate the effective torque, M_i, consider the following argument. Rather than the configuration depicted on the left of Fig. S7, let us consider the situation sketched on the right, where each $+1/2$ disclination has been replaced by a $\pm 1/2$ disclination dipole. The energy of such a configuration is given by

$$E = -2\pi K \sum_{i<j}^{1,4} k_i k_j \log \frac{|\boldsymbol{r}_i - \boldsymbol{r}_j|}{a} + 4E^{\text{self}} \ , \tag{13}$$

where a is the core radius, K the Frank constant, $k = \pm 1/2$ the turning number and E_{self} the position-independent self-energy of the defects. Calculating the interaction energy gives

$$\begin{aligned} \frac{E^{\text{int}}}{2\pi k^2 K} &= \log|\boldsymbol{r}_1^+ - \boldsymbol{r}_1^-| + \log|\boldsymbol{r}_1^+ - \boldsymbol{r}_2^-| - \log|\boldsymbol{r}_1^+ - \boldsymbol{r}_2^+| \\ &\quad - \log|\boldsymbol{r}_1^- - \boldsymbol{r}_2^-| + \log|\boldsymbol{r}_1^- - \boldsymbol{r}_2^+| + \log|\boldsymbol{r}_2^+ - \boldsymbol{r}_2^-| \, . \end{aligned}$$

Now introduce explicitly the orientation of the dipoles by taking $\boldsymbol{r}_i^+ = \boldsymbol{r}_i$ and $\boldsymbol{D}_i = \boldsymbol{r}_i^+ - \boldsymbol{r}_i^-$, with $i = 1,\ 2$. Furthermore, let $\boldsymbol{D}_i = D_i \boldsymbol{u}_i$ and take $D_1 = D_2$ for simplicity. With these manipulations the interaction energy becomes

$$\begin{aligned} \frac{E^{\text{int}}}{2\pi k^2 K} &= 3\log D - \log|\boldsymbol{r}_1 - \boldsymbol{r}_2| + \log\left|\frac{\boldsymbol{r}_1 - \boldsymbol{r}_2}{D} - \boldsymbol{u}_1\right| \\ &\quad + \log\left|\frac{\boldsymbol{r}_2 - \boldsymbol{r}_1}{D} - \boldsymbol{u}_2\right| - \log\left|\frac{\boldsymbol{r_1} - \boldsymbol{r}_2}{D} - \boldsymbol{u}_1 + \boldsymbol{u}_2\right| \, . \end{aligned} \tag{14}$$

The case of two $+1/2$ disclinations can be recovered by taking $|\boldsymbol{r}_1 - \boldsymbol{r}_2|/D \ll 1$. Thus replacing E^{int} in the expression for the energy and neglecting irrelevant constants we obtain

$$E = -2\pi k^2 K \left[\log\frac{|\boldsymbol{r}_1 - \boldsymbol{r}_2|}{a} + \frac{1}{2}\log\left(1 - \boldsymbol{u}_1 \cdot \boldsymbol{u}_2\right)\right] \, . \tag{15}$$

The elastic torque acting on $\boldsymbol{u}_i$ is evidently $M_i = -\partial E/\partial\psi_i$. Thus the dynamical equation for the angle ψ_i, generalized to the case of an arbitrary number of $+1/2$ defects, is given by

$$\zeta_r \frac{d\psi_i}{dt} = -\pi k^2 K \sum_{i<j} \frac{\boldsymbol{u}_i^{\perp} \cdot \boldsymbol{u}_j}{1 - \boldsymbol{u}_i \cdot \boldsymbol{u}_j} = \pi k^2 K \sum_{i<j} \cot\left(\frac{\psi_i - \psi_j}{2}\right) \, . \tag{16}$$

As a consequence, two disclinations with parallel symmetry axes will experience a diverging restoring torque, while the torque is zero if the disclinations are anti-parallel (i.e. $\psi_i - \psi_j = \pi$) as one would expect. In the case of $+1/2$ disclinations on a curved surface, the construction described here can be repeated, but the lines $\boldsymbol{D}_i$ connecting the the positive and negative disclinations must be replaced by geodesic curves.

Figs. S1 to S8

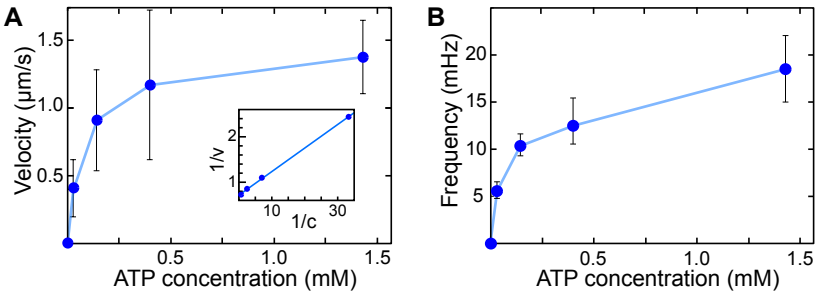

Fig. S1: ATP concentration controls defect velocity and frequency of oscillations. (A) Defect velocity v increases with ATP concentration c. The inset shows an inverse plot with a linear fit, suggesting that the Michaelis-Menten kinetics of kinesin is transmitted to the defect movement. **(B)** Dependence of oscillation frequency, determined by peak counting in the angular distances of the defects, on the ATP concentration. Error bars indicate the determined standard deviation (A) and estimated error (B).

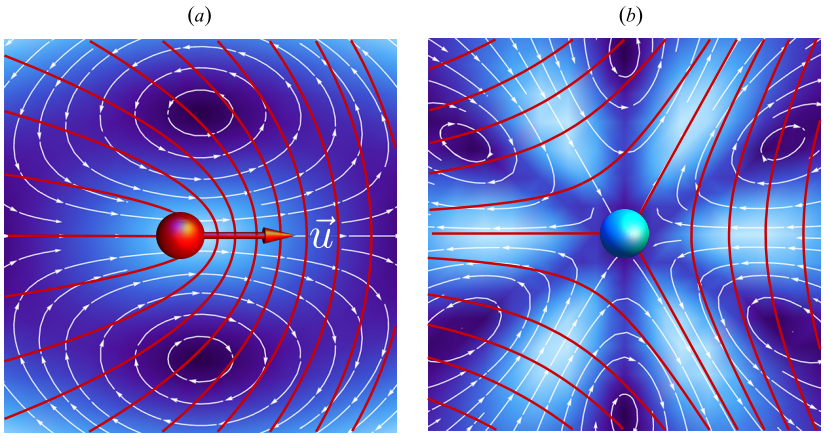

Fig. S2: Spontaneous flow by active nematic disclinations. The flow produced by $\pm 1/2$ disclinations in a two-dimensional extensile active nematic medium. The white streamlines indicate the flow velocity while the red lines mark the nematic director. The head-tail structure of $+1/2$ disclinations gives the flow a specific directionality that in extensile systems results in a net motion of the defect core towards the head.

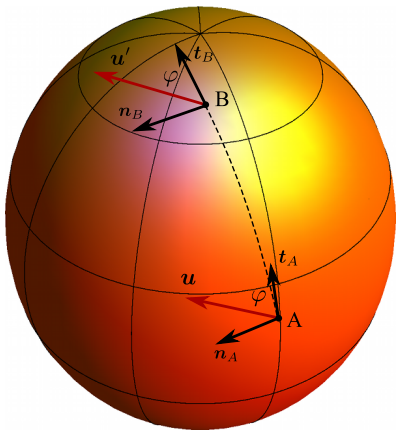

Fig. S3: A graphic representation of the concept of parallel transport. A tangent vector $\boldsymbol{u}$ (in red) is transported from point A to point B along a great circle. Along the whole path the vector forms a constant angle φ with respect to the path tangent vector.

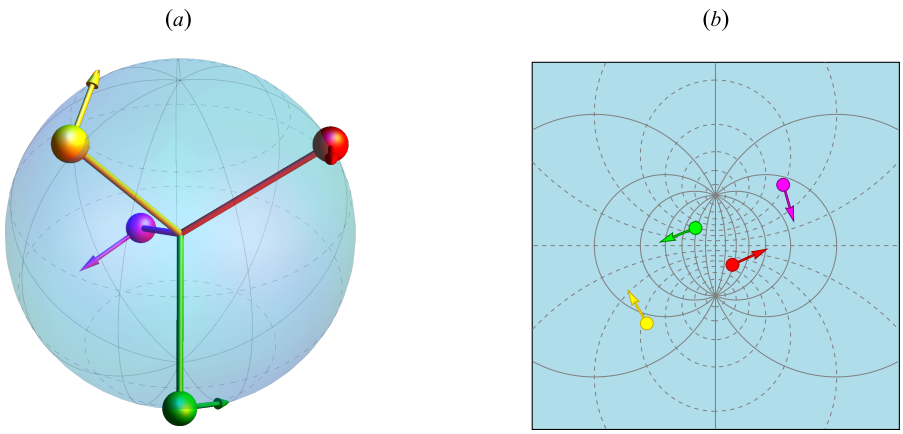

Fig. S4: Tetrahedral configuration of defects on the sphere. (*a*) The "baseball" configuration obtained from a numerical solution of Eqs. (6) and (8) in the case $v_0 = 0$. (*b*) a stereographic projection of the same configuration.

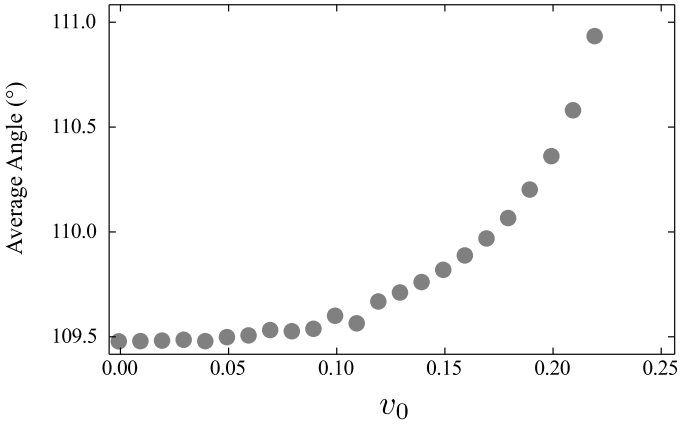

Fig. S5: Distorted tetrahedral configuration. The average angle $\langle\alpha\rangle$, as defined in Eq. (10), for increasing v_0 values obtained from a numerical solution of Eqs. (6) and (8). The angle exhibits a rapid increase as the value $v_0^* \approx 0.25$ is approached. This marks the instability of the (distorted) tetrahedral configuration to the oscillatory regime.

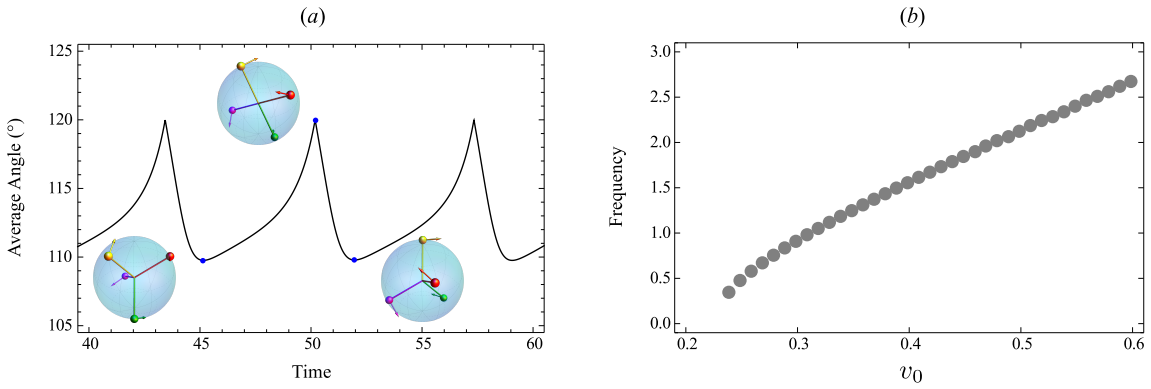

Fig. S6: Spontaneous oscillations of defective configurations. (a) Average angle versus time obtained from a numerical integration of Eqs. (6) and (8) for $\Gamma = 3$ and $v_0 = 0.3$. The insets show the defects oscillating between two symmetric tetrahedral configurations (left and right) through an intermediate planar configuration (center). (b) The frequency of the oscillations versus v_0 obtained from a numerical integration of Eqs. (6) and (8) for $\Gamma = 40$.

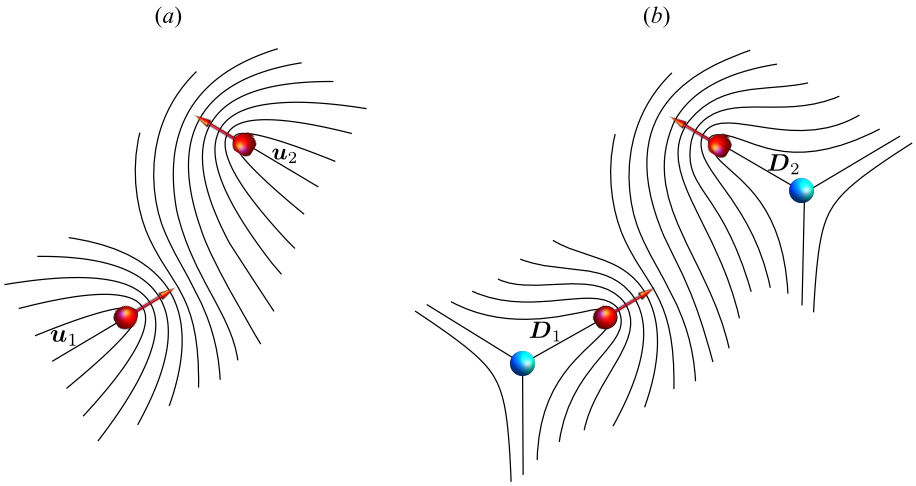

Fig. S7: Orientational interaction between $+1/2$ disclinations. (a) two $+1/2$ disclinations next to each other. Due to the reorientation of the director field, their symmetry axes will experience an effective torque. (b) The same configuration after replacing the $+1/2$ disclinations with $\pm 1/2$ dipoles. The previous configuration is obtained by letting the distance D between the positive and negative disclination in the dipole go to infinity.

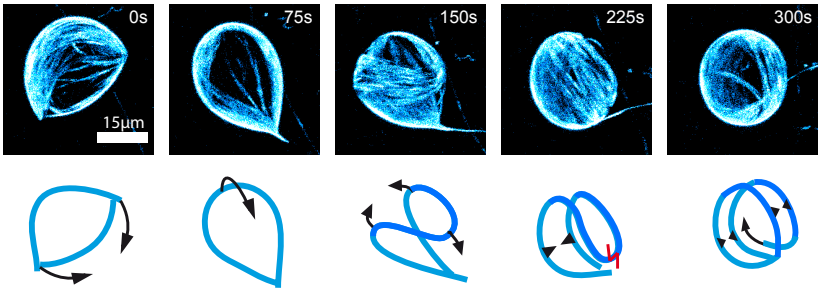

Fig. S8: Transition from spindle shape to ring mode. Confocal images showing the z-projection of the vesicle shape, with corresponding schematics. A spindle onfiguration (t=0s) transforms into a spike configuration by merging of the two poles (t=75s). The transport (t=150s), breakage (t=225s), and subsequent annealing (t=300s) of the microtubules results in a ring configuration.

Captions for Movies S1 to S8

Movie S1:

Dynamics of nematic defects confined on a spherical vesicle. The left panels show the z-projected hemispheres (as explained in Figure 1a of the main text). The microtubule bundles are shown in cyan and the positions of the four $+1/2$ defects are indicated by the colored markers (magenta, red, yellow, green). The right panel shows the reconstructed 3D-view of the defect dynamics within a unit sphere.

Movie S2:

Theoretical model predicts oscillatory dynamics of four $+1/2$ defects confined on a spherical surface. The left panel shows a 3D-view of the defect movement from numerical simulations. A stereographic projection is given at the upper right. The defect positions r_i are marked by the dots and the arrows represent the orientation u_i. The corresponding state in the energy landscape is shown on the lower right (violet dot).

Movie S3:

Active nematic cortex drives vesicle-shape changes. For membranes with excess membrane area, the active nematic cortex induces significant shape deformation. The vesicle is locally elongated along the direction of the four $+1/2$ defects oscillatory motion.

Movie S4:

Deformations of deflated vesicles with excess membrane. An initially round vesicle undergoes elliptic shape deformation as excess membrane is provided. Protrusions grow out at the positions of the defects. The ring pattern is an artifact of the imaging due to the fact that the $z-$resolution was reduced to increase the frame rate. A median filter was applied to reduce the noise. At $t = 5$ min and 25 s the hypertonic stress was applied, which resulted in a drift of the vesicle and the subsequent correction of the sample position.

Movie S5:

Ring-mode vesicle. The microtubule nematic forms a rotating ring inside the vesicle. The ring elongates and folds into a structure with four defects that move pairwise towards each other. By the collision of the defects a new ring is formed and the process repeats itself.

Movie S6:

Ring-mode schematic. The schematic illustrates the elongation and folding of the ring described in Movie S5.

Movie S7:

Spindle-like vesicle. The movie displays the dynamics of a spindle-like vesicle with two $+1$ defects at its poles. The bundles at the poles extend and create stresses that cause the spindle to flip and fold onto itself as the two poles merge together. Bundles then protrude at the opposite side creating a new pole and thus the process starts to repeat.

Movie S8:

Spindle-like vesicle that transforms into a ring. The two poles of an initial spindle configuration ($t = 0$ s) merge into a spike ($t = 75$ s). The transport ($t = 150$ s), breakage ($t = 225$ s), and subsequent annealing ($t = 300$ s) of the microtubules results in a ring configuration.

References and Notes:

1. L. S. Penrose, Dermatoglyphic topology. *Nature* **205**, 544-546 (1965)10.1038/205544a0).

2. T. C. Lubensky, J. Prost, Orientational order and vesicle shape. *J. de Physique* **2**, 371-382 (1992).

3. D. R. Nelson, Toward a tetravalent chemistry of colloids. *Nano Lett.* **2**, 1125-1129 (2002); published online EpubOct (10.1021/nl0202096).

4. T. Lopez-Leon, V. Koning, K. B. S. Devaiah, V. Vitelli, A. Fernandez-Nieves, Frustrated nematic order in spherical geometries. *Nat. Phys.* **7**, 391-394 (2011); published online EpubMay (10.1038/nphys1920).

5. H. Shin, M. J. Bowick, X. J. Xing, Topological defects in spherical nematics. *Phys. Rev. Lett.* **101**, (2008); published online EpubJul (10.1103/PhysRevLett.101.037802).

6. V. Vitelli, D. R. Nelson, Nematic textures in spherical shells. *Phys. Rev. E* **74**, (2006); published online EpubAug (10.1103/PhysRevE.74.021711).

7. P. Poulin, H. Stark, T. C. Lubensky, D. A. Weitz, Novel colloidal interactions in anisotropic fluids. *Science* **275**, 1770-1773 (1997); published online EpubMar (10.1126/science.275.5307.1770).

8. I. Musevic, M. Skarabot, U. Tkalec, M. Ravnik, S. Zumer, Two-dimensional nematic colloidal crystals self-assembled by topological defects. *Science* **313**, 954-958 (2006); published online EpubAug (10.1126/science.1129660).

9. A. R. Bausch *et al.*, Grain boundary scars and spherical crystallography. *Science* **299**, 1716-1718 (2003); published online EpubMar (10.1126/science.1081160).

10. W. T. M. Irvine, V. Vitelli, P. M. Chaikin, Pleats in crystals on curved surfaces. *Nature* **468**, 947-951 (2010); published online EpubDec (10.1038/nature09620).

11. C. P. Lapointe, T. G. Mason, Smalyukh, II, Shape-Controlled Colloidal Interactions in Nematic Liquid Crystals. *Science* **326**, 1083-1086 (2009); published online EpubNov (10.1126/science.1176587).

12. B. Senyuk, *et al.*, Topological colloids. *Nature* **493**, 200-205 (2013); published online EpubJan (10.1038/nature11710).

13. I. H. Lin, D. S. Miller, P. J. Bertics, C. J. Murphy, J. J. de Pablo, N. L. Abbott, Endotoxin-Induced Structural Transformations in Liquid Crystalline Droplets. *Science* **332**, 1297-1300 (2011); published online EpubJun (10.1126/science.1195639).

14. J. A. Moreno-Razo, E. J. Sambriski, N. L. Abbott, J. P. Hernandez-Ortiz, J. J. de Pablo, Liquid-crystal-mediated self-assembly at nanodroplet interfaces. *Nature* **485**, 86-89 (2012); published online EpubMay (10.1038/nature11084).

15. P. Lipowsky, M. J. Bowick, J. H. Meinke, D. R. Nelson, A. R. Bausch, Direct visualization of dislocation dynamics in grain-boundary scars. *Nat. Mat.* **4**, 407-411 (2005); published online EpubMay (10.1038/nmat1376).

16. G. N. Meng, J. Paulose, D. R. Nelson, V. N. Manoharan, Elastic Instability of a Crystal Growing on a Curved Surface. *Science* **343**, 634-637 (2014); published online EpubFeb (10.1126/science.1244827).

17. U. Tkalec, M. Ravnik, S. Copar, S. Zumer, I. Musevic, Reconfigurable Knots and Links in Chiral Nematic Colloids. *Science* **333**, 62-65 (2011); published online EpubJul (10.1126/science.1205705).

18. S. Zhou, A. Sokolov, O. D. Lavrentovich, I. S. Aranson, Living liquid crystals. *Proc. Nat. Acad. Sci. U.S.A.*, 1265-1270 (2014); published online EpubJan (10.1073/pnas.1321926111).

19. T. Sanchez, D. T. N. Chen, S. J. DeCamp, M. Heymann, Z. Dogic, Spontaneous motion in hierarchically assembled active matter. *Nature* **491**, 431-+ (2012); published online EpubNov (10.1038/nature11591).

20. G. Duclos, S. Garcia, H. G. Yevick, P. Silberzan, Perfect nematic order in confined monolayers of spindle-shaped cells. *Soft Matter* **10**, 2346-2353 (2014)10.1039/c3sm52323c).

21. L. Giomi, M. J. Bowick, X. Ma, M. C. Marchetti, Defect annihilation and proliferation in active nematics. *Phys. Rev. Lett.* **110**, 228101 (2013).

22. S. P. Thampi, R. Golestanian, J. M. Yeomans, Velocity Correlations in an Active Nematic. *Phys. Rev. Lett.* **111**, (2013); published online EpubSep (10.1103/PhysRevLett.111.118101).

23. T. Gao, R. Blackwell, M. Glaser, M. Betterton, M. Shelley, A multiscale active nematic theory of microtubule/motor-protein assemblies. http://arxiv.org/abs/1401.8059, (2014).

24. J. Palacci, S. Sacanna, A. P. Steinberg, D. J. Pine, P. M. Chaikin, Living Crystals of Light-Activated Colloidal Surfers. *Science* **339**, 936-940 (2013); published online EpubFeb (10.1126/science.1230020).

25. M. Abkarian, E. Loiseau, G. Massiera, Continuous droplet interface crossing encapsulation (cDICE) for high throughput monodisperse vesicle design. *Soft Matter* **7**, 4610-4614 (2011)10.1039/c1sm05239j).

26. S. Asakura, F. Oosawa, On interaction between 2 bodies immersed in a solution of macromolecules. *J. Chem. Phys.* **22**, 1255-1256 (1954).

27. M. J. Schnitzer, S. M. Block, Kinesin hydrolyses one ATP per 8-nm step. *Nature* **388**, 386-390 (1997); published online EpubJul (10.1038/41111).

28. C. Hentrich, T. Surrey, Microtubule organization by the antagonistic mitotic motors kinesin-5 and kinesin-14. *J. Cell Biol.* **189**, 465-480 (2010); published online EpubMay (10.1083/jcb.200910125).

29. T. Surrey, F. Nedelec, S. Leibler, E. Karsenti, Physical properties determining self-organization of motors and microtubules. *Science* **292**, 1167-1171 (2001); published online EpubMay (10.1126/science.1059758).

30. Materials and methods are available as supplementary material on Science Online.

31. R. Voituriez, J. F. Joanny, J. Prost, Spontaneous flow transition in active polar gels. *EPL* **70**, 404-410 (2005); published online EpubMay (10.1209/epl/i2004-10501-2).

32. D. Marenduzzo, E. Orlandini, M. E. Cates, J. M. Yeomans, Steady-state hydrodynamic instabilities of active liquid crystals: Hybrid lattice Boltzmann simulations. *Phys. Rev. E* **76**, (2007); published online EpubSep (10.1103/PhysRevE.76.031921).

33. R. A. Simha, S. Ramaswamy, Hydrodynamic fluctuations and instabilities in ordered suspensions of self-propelled particles. *Phys. Rev. Lett.* **89**, (2002); published online EpubJul (10.1103/PhysRevLett.89.058101).

34. T. S. Nguyen, J. Geng, R. L. B. Selinger, J. V. Selinger, Nematic order on a deformable vesicle: theory and simulation. *Soft Matter* **9**, 8314-8326 (2013)10.1039/c3sm50489a).

35. M. Elbaum, D. K. Fygenson, A. Libchaber, Buckling microtubules in vesicles. *Phys. Rev. Lett.***76**, 4078-4081 (1996); published online EpubMay (10.1103/PhysRevLett.76.4078).

36. P. Prinsen, P. van der Schoot, Shape and director-field transformation of tactoids. *Phys. Rev. E* **68**, (2003); published online EpubAug (10.1103/PhysRevE.68.021701).

37. E. Abu Shah, K. Keren, Symmetry breaking in reconstituted actin cortices. *Elife* **3**, (2014); published online EpubApr (10.7554/eLife.01433).

38. H. Baumann, T. Surrey, Motor-Mediated Cortical versus Astral Microtubule Organisation in Lipid-Monolayered Droplets *J. Biol. Chem.*, (2014) doi:10.1074/jbc.M114.58201).

39. M. Pinot, F. Chesnel, J. Z. Kubiak, I. Arnal, F. J. Nedelec, Z. Gueroui, Effects of Confinement on the Self-Organization of Microtubules and Motors. *Curr. Biol.* **19**, 954-960 (2009); published online EpubJun (10.1016/j.cub.2009.04.027).

40. E. Tjhung, D. Marenduzzo, M. E. Cates, Spontaneous symmetry breaking in active droplets provides a generic route to motility. *Proc. Nat. Acad. Sci. U.S.A.* **109**, 12381-12386 (2012); published online EpubJul (10.1073/pnas.1200843109).